

Geochronology, geochemistry, and Sr–Nd isotopes of Early Carboniferous magmatism in southern West Junggar, northwestern China: Implications for Junggar oceanic plate subduction

LIU Pengde¹, LIU Xijun^{1,2,3*}, XIAO Wenjiao², ZHANG Zhiguo¹, SONG Yujia¹, XIAO Yao¹, LIU Lei^{1,2,3}, HU Rongguo¹, WANG Baohua^{1,3}

¹ Guangxi Key Laboratory of Hidden Metallic Ore Deposits Exploration, College of Earth Sciences, Guilin University of Technology, , Guilin 541004, China;

² Xinjiang Research Center for Mineral Resources, Xinjiang Institute of Ecology and Geography, Chinese Academy of Sciences, Urumqi 830011, China;

³ Collaborative Innovation Center for Exploration of Nonferrous Metal Deposits and Efficient Utilization of Resource, Guilin University of Technology, Guilin 541004, China

Abstract: West Junggar is a key area for understanding intra-oceanic plate subduction and the final closure of the Junggar Ocean. Knowledge of the Carboniferous tectonic evolution of the Junggar Ocean region is required for understanding the tectonic framework and accretionary processes in West Junggar, Central Asian Orogenic Belt. A series of Early Carboniferous volcanic and intrusive rocks, namely, basaltic andesite, andesite, dacite, and diorite, occur in the Mayile area of southern West Junggar, northwestern China. Our new LA-ICPMS zircon U–Pb geochronological data reveal that diorite intruded at 334 (±1) Ma, and that basaltic andesite was erupted at 334 (±4) Ma. These intrusive and volcanic rocks are calc-alkaline, display moderate MgO (1.62%–4.18%) contents and Mg# values (40–59), and low Cr (14.5×10^{-6} – 47.2×10^{-6}) and Ni (7.5×10^{-6} – 34.6×10^{-6}) contents, and are characterized by enrichment in light rare-earth elements and large-ion lithophile elements and depletion in heavy rare-earth elements and high-field-strength elements, meaning that they belong to typical subduction-zone island-arc magma. The samples show low initial $^{87}\text{Sr}/^{86}\text{Sr}$ ratios (range of 0.703649–0.705008), positive $\epsilon_{\text{Nd}(t)}$ values (range of 4.8–6.2 and mean of 5.4), and young T_{DM} Nd model ages ranging from 1016 to 616 Ma, indicating a magmatic origin from depleted mantle involving partial melting of 10%–25% garnet and spinel lherzolite. Combining our results with those of previous studies, we suggest that these rocks were formed as a result of northwestward subduction of the Junggar oceanic plate, which caused partial melting of sub-arc mantle. We conclude that intra-oceanic arc magmatism was extensive in West Junggar during the Early Carboniferous.

Keywords: Early Carboniferous magmatism; geochronology; geochemistry; Junggar Oceanic plate subduction; West Junggar; Central Asian Orogenic Belt

*Corresponding author: LIU Xijun (E-mail: xijunliu@glut.edu.cn)

Received 2020-10-31; revised 2021-06-01; accepted 2021-06-15

© Xinjiang Institute of Ecology and Geography, Chinese Academy of Sciences, Science Press and Springer-Verlag GmbH Germany, part of Springer Nature 2021

1 Introduction

The Central Asian Orogenic Belt (CAOB) (Jahn et al., 2000a, b) extends from the Urals in the west through Kazakhstan, northwestern China, Mongolia, and northeastern China to the Russian Far East (Windley et al., 2007; Xiao et al., 2010a; Xu et al., 2013, 2015). It is generally accepted that the CAOB comprises a complicated and varied collage of terranes, including island arcs, ophiolites, accretionary prisms, seamounts, and microcontinents (Windley et al., 2007; Kröner et al., 2008; Xiao et al., 2008a). The CAOB is the world's largest accretionary orogen (Sengör et al., 1993; Windley et al., 2007; Xiao et al., 2010b; Safonova et al., 2011, 2015, 2016) and is also considered a type area for studying Phanerozoic continental growth (Sengör et al., 1993; Jahn et al., 2004; Xiao and Santosh, 2014; Xiao et al., 2015). The accretionary processes of the orogen might have resulted from either the progressive duplication of a single and long-lived island-arc system (Sengör et al., 1993; Sengör and Natal'in, 1996) or the collision of several island arcs and microcontinents, similar to the complex archipelago systems in the modern southwestern Pacific (Filippova et al., 2002; Khain et al., 2003; Yakubchuk et al., 2005; Windley et al., 2007; Xiao et al., 2010b).

West Junggar is located in a key area of the CAOB, at the junction of the Siberia, Kazakhstan, and Tianshan orogens, and has thus been a focus of studies of the tectonic evolution and crustal growth of the orogenic belt (Coleman, 1989; Feng et al., 1989; Xiao et al., 2008b). Based on the regional geology, West Junggar has been considered by some geologists as a paleo intra-oceanic subduction system (Xiao et al., 2008b; Zhang et al., 2011), whereas others have variously argued that West Junggar was formed by single subduction (Wang et al., 2003), arc-arc collision (Buckman and Aitchison, 2004), or ridge subduction (Geng et al., 2009; Tang et al., 2010; Yin et al., 2010, 2011), or by post-collisional processes after the Early Carboniferous (Han et al., 2010), seamounts/oceanic plateaus subduction and accretion model (Yang et al., 2015; Zhang et al., 2018; Du et al., 2019; Yang et al., 2020). An understanding of the Carboniferous tectonic setting is critical for determining the evolution of West Junggar (Chen and Jahn, 2004; Chen and Arakawa, 2005; Geng et al., 2009).

West Junggar is considered a key area for understanding intra-oceanic plate subduction and the final closure of the Junggar Ocean (a major southern branch of the paleo-Asian Ocean) during the Carboniferous (Coleman, 1989; Feng et al., 1989; Buckman and Aitchison, 2004; Windley et al., 2007; Xiao et al., 2010a). Some studies have suggested an Early Carboniferous age for the final closure of the Junggar Ocean (Gao et al., 1998), whereas others have argued for the Late Carboniferous (Chen et al., 2010; Han et al., 2010; Zhang et al., 2011) or Permian (Xiao et al., 2008b; Geng et al., 2009; Tang et al., 2010). Knowledge of the timing of oceanic closure and tectonic transition is not only critical for deciphering the geological history of West Junggar, but also important for understanding the processes of continental crustal growth. Therefore, although previous studies have comprehensively investigated Carboniferous magmatic rocks in West Junggar (Jahn et al., 2000a; Chen and Jahn, 2004; Chen and Arakawa, 2005; Geng et al., 2009), the tectonic setting and timing of geodynamic processes of this region remain uncertain.

Early Carboniferous volcanic and intrusive rocks are widely exposed in the Mayile area in southern West Junggar. These rocks should place important constraints on the evolution of the Junggar Ocean region because they formed during different stages of evolution and might have been derived from different sources. There has been little geochemical or geochronological research into these rocks, partly because of a lack of accessibility. Here, we focus on the Mayile volcanic and intrusive rocks from the southern West Junggar region and, on the basis of our new geochronological, major- and trace-element, and Sr–Nd isotopic data, establish the formation age and petrogenesis of these igneous rocks, and constrain their tectonic setting.

2 Geological setting

West Junggar (44°50'–47°13'N, 82°16'–86°34'E) lies along the border between northwestern China and Kazakhstan, and is surrounded by the Junggar Basin, the Kazakhstan plate, and the

Tianshan and Altay Orogenes (Feng et al., 1989; Chen and Jahn, 2004; Choulet et al., 2013). No Precambrian basement has been documented in this area, and the oldest rocks are ophiolitic mafic-ultramafic types of Cambrian-Ordovician age (Coleman, 1989; Feng et al., 1989; Buckman and Aitchison, 2004) (Fig. 1). West Junggar is composed of Paleozoic volcanic arcs and accretionary complexes (Windley et al., 2007; Xiao et al., 2008a). These accretionary complexes are composed of Ordovician to lower Carboniferous volcano-sedimentary rocks. The Ordovician and Silurian strata are distributed mainly in southwestern West Junggar, and the Carboniferous strata in the southeast (Fig. 1), with these units incorporating extensive volcanic rocks (Yang et al., 2012). West Junggar can be tectonically divided into northern and southern parts by the Xiemisitai Fault. Northern West Junggar consists of the Zharma-Saur and Boshchekul-Chingiz arcs. Southern West Junggar contains extensively deformed ophiolitic mélange, as well as large fault-blocks of volcanic-sedimentary strata, which have been modified by the post-Permian Barleik, Mayile, and Darbut strike-slip faults (Fig. 1). The Silurian sandstone and Carboniferous basaltic rocks are intruded by Early Carboniferous quartz monzonite, biotite granite, and diorite in southern West Junggar (XBGMR, 1993).

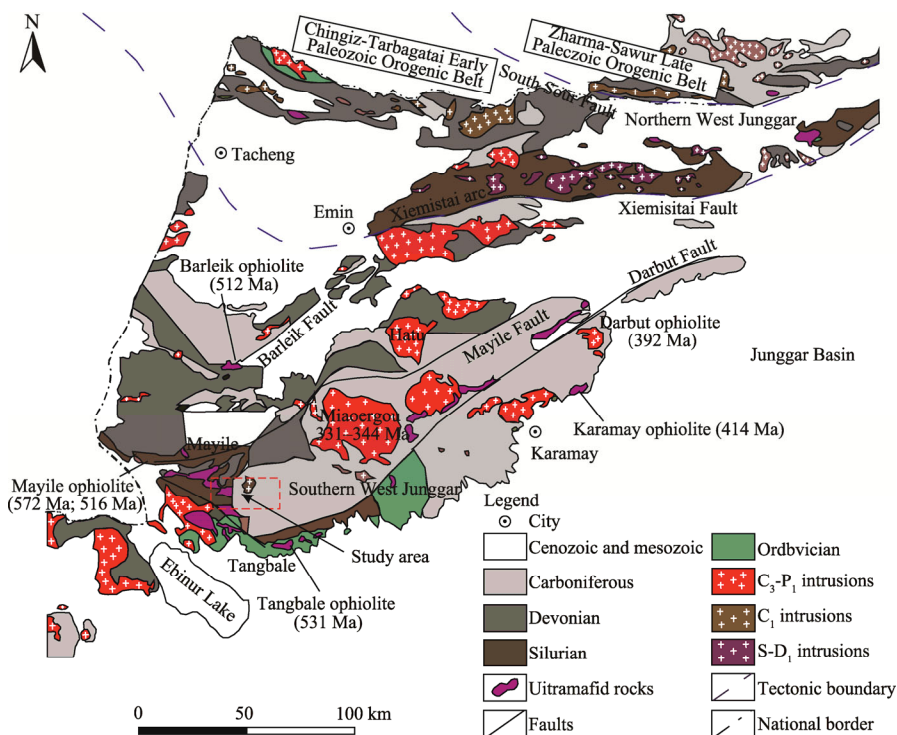


Fig. 1 Geological map of West Junggar region (modified after Xiao et al. (2009), Yang et al. (2012), and Yang et al. (2019)). Age data are from Jian et al. (2005), Xu et al. (2006), Gu et al. (2009), Geng et al. (2011), Yang et al. (2012), and Ren et al. (2014).

Carboniferous volcanic and intrusive rocks are widespread throughout southeastern West Junggar, near the Mayile ophiolitic mélange that formed an important Early Carboniferous volcanic arc. In the study area, the exposed strata comprise mainly the Late Carboniferous Qierqusitao (C_2q) and the Middle Devonian Kulumudi (D_2k) formations (Fig. 2). The Qierqusitao Formation is composed of clastic rocks, quartz sandstone, siltstone, siliceous rock, ultramafic rock, basalt, and basaltic andesite. The Kulumudi Formation comprises sandstone, detrital sandstone, tuff, andesite, volcaniclastic rocks, basic and intermediate-felsic volcanic rocks, local limestone, rhyolite, trachyte, and andesite. In addition, a few intermediate-felsic dikes are exposed in the area, including a Carboniferous-middle Permian batholith, quartz diorite porphyry, diorite porphyry, and granite-diorite, as well as post-collisional granites. The volcanic and intrusive rocks in this study are come from Qierqusitao (C_2q) Formation.

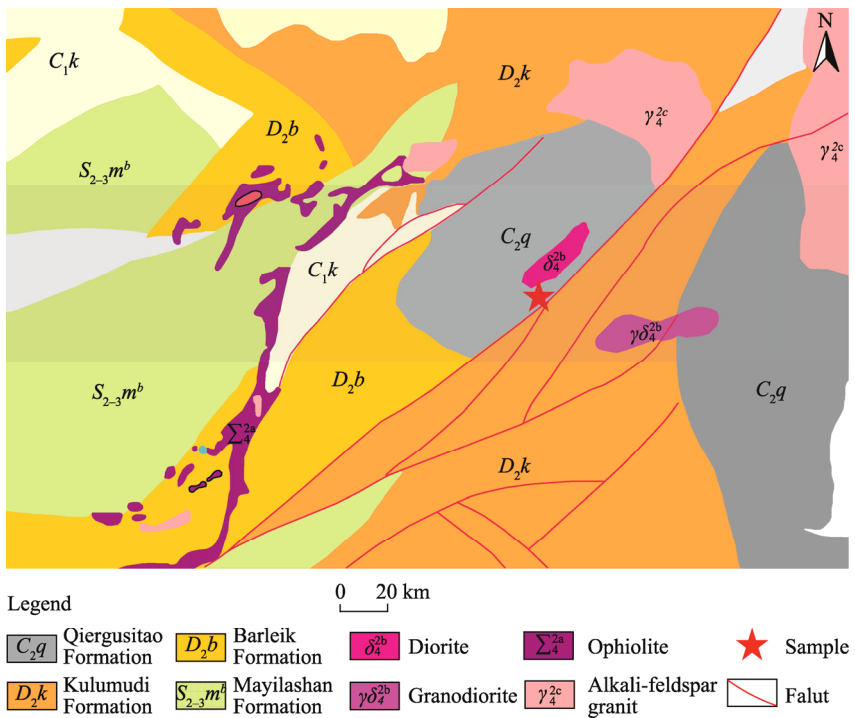


Fig. 2 Simplified geological map of Mayile area

3 Petrography

Representative samples of magmatic rocks were selected from the Mayile area during our field trip in August 2019 (Fig. 2), including andesites, basaltic andesites, diorites, and dacites. The petrography of the individual lithological samples is described briefly below (Figs. 3 and 4).

Andesites are porphyritic, containing <5% phenocryst of plagioclase and pyroxene. The groundmass has aphanitic texture and is composed of tiny plagioclase and pyroxene (Figs. 3a, 3b, and 4a).

Basaltic andesites are dark gray and porphyritic, containing with 15%–25% plagioclase and pyroxene phenocrysts that are set in a matrix of microcrystalline plagioclase (40%) and pyroxene (20%) with minor intergranular magnetite (<5%). Plagioclase phenocrysts are platy shapes and 0.2–0.8 mm long (Figs. 3c and 4b).

Diorites contain plagioclase (60%–70%), hornblende (5%–10%), and minor Fe–Ti-oxides (<3%). Plagioclase phenocrysts are euhedral and commonly altered to smectite and albite. Hornblende occurs as subhedral grains with slight chloritization (Figs. 3d and 4c).

Dacites contain <5% phenocrysts of plagioclase and quartz. The groundmass has in a pilotaxitic texture and contains 75% microcrystal plagioclase, 5% quartz, and some glass (Figs. 3e and 4d).

4 Methods

The U–Pb zircon dating, major elements, trace elements, and Sr and Nd isotope analyses were carried out at the Guangxi Key Laboratory of Hidden Metallic Ore Deposits Exploration, Guilin University of Technology, Guilin City, Guangxi Zhuang Autonomous Region, China.

4.1 Zircon U–Pb geochronology

Zircon grains were obtained from samples 19MY-03 (basaltic andesite) and 19MY-05 (diorite) using conventional heavy-liquid and magnetic methods and then mounted in epoxy resin discs and polished with 0.25 μm diamond paste to section the crystals in half. All of the zircon grains

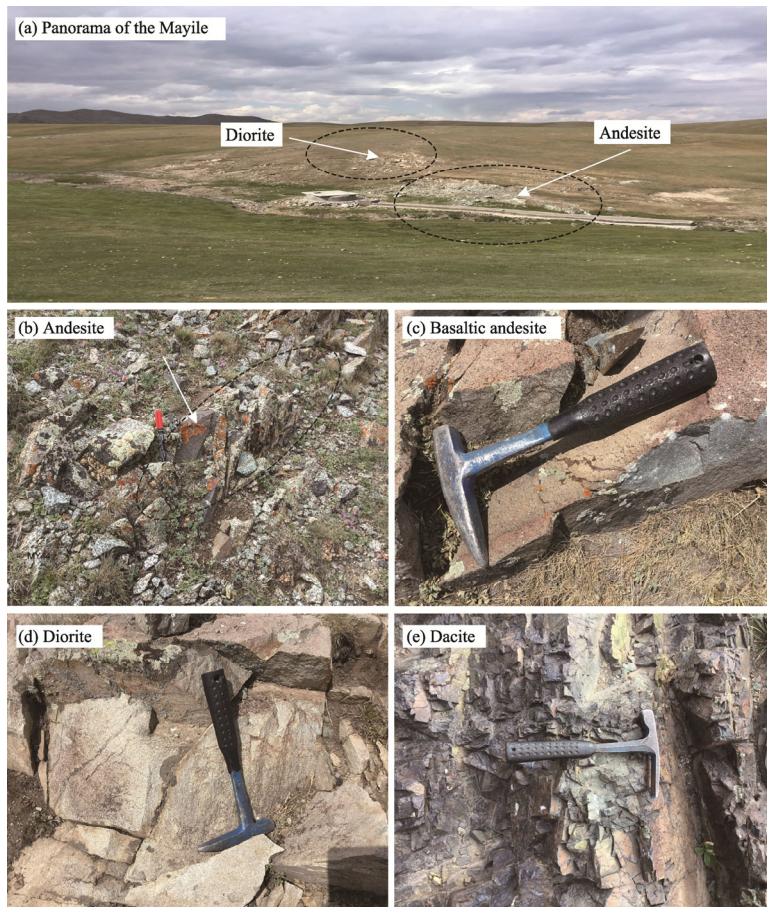


Fig. 3 Typical field photographs of Mayile magmatic rocks. (a), panorama of Mayile; (b), andesite; (c), basaltic andesite; (d), diorite; (e), dacite.

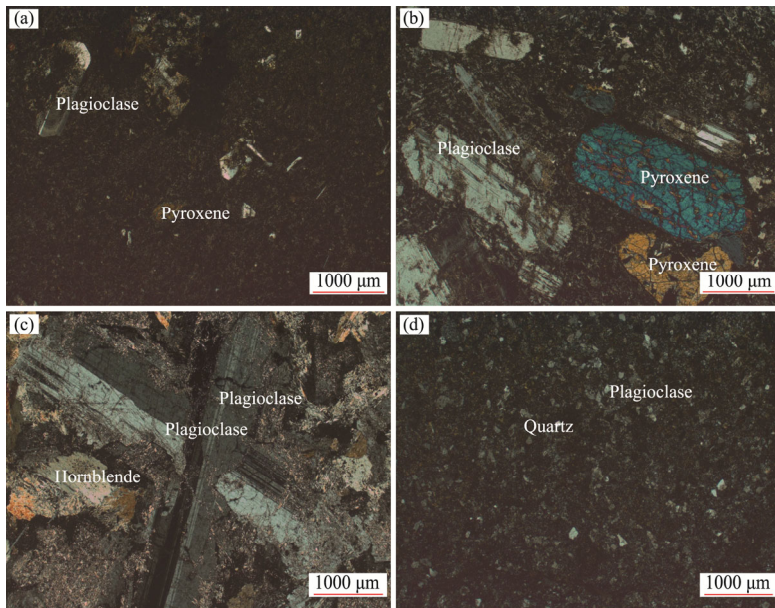


Fig. 4 Representative photomicrographs of different Mayile magmatic rocks. (a), andesite; (b), basaltic andesite; (c), diorite; (d), dacite.

selected for analysis were documented with transmitted- and reflected-light photomicrographs as well as cathodoluminescence (CL) images to reveal their internal structures. The CL imaging was performed using a JXA8230R electron microprobe (JEOL Ltd., Mitaka, Japan). Laser ablation-inductively coupled plasma-mass spectrometry (LA-ICP-MS) U-Pb zircon dating was conducted using a Agilent quadrupole 7900 ICP-MS instrument (Agilent Technologies Inc., CA, USA) coupled to a GeoLas HD LA system (Coherent Inc., CA, USA) equipped with a 193 nm ArF-excimer laser with an automatic positioning system. The laser spot size was set to 24 μm . The counting time was 50 s for U, Th, ^{204}Pb , ^{206}Pb , ^{207}Pb , and ^{208}Pb , and 30 s for other elements. Calibrations for the zircon analyses involved United States National Institute of Standards and Technology (NIST) Standard Reference Material NIST610 glass as an external standard and Si as an internal standard. The U-Pb isotope fractionation effects were corrected using zircon Plesovice (Liu et al., 2020) as an external standard. ICPMSDataCal software was used to process the ablated signal data and to obtain trace-element contents and U-Pb isotope ratios of the samples. Concordia ages and diagrams were obtained using Isoplot/Ex (Ludwig, 2003).

4.2 Major- and trace-element analyses

Fresh rock samples (10 samples) were selected, avoiding or removing weathered surfaces, and crushed into small chips. Any strongly altered chips and secondary vein materials were removed, and the remaining chips were soaked in 4N hydrochloric acid for 30 min to leach out alteration minerals. The rock chips were then powdered using an alumina ceramic shatterbox. Major-element contents were determined using a ZSX Primus II X-ray fluorescence (XRF) instrument (Rigaku, Tokyo, Japan) at the Guangxi Key Laboratory of Hidden Metallic Ore Deposits Exploration, Guilin University of Technology, Guilin, China. The loss on ignition (LOI) of each sample was measured before the glass frit measurement, and the sample after calcination was used for analysis. The glass frit was measured on a ZSX Primus II XRF instrument.

Trace-element analyses were performed on an Agilent 7500CX ICP-MS instrument (Agilent Technologies Inc., CA, USA) using the acid-solution method. About 50 mg of sample powder and standard sample (The United States Geological Survey standards BHVO, AGV, W-2, and G-2 and national rock standards GSR-1, GSR-2, and GSR-3) was placed in a bomb, and 0.5 mL of purified HNO_3 and 1.0 mL of purified HF. The bomb was placed in a high-pressure valve and maintained at 190°C for 48 h in a constant-temperature electric heating box. After evaporation to dryness, 0.5 mL of purified HNO_3 was added, with this step being repeated again. A volume of 4 mL of 4N purified HNO_3 was then added. The high-pressure valve was placed in a thermostatic electric oven at 170°C for 4 h. Finally, the solution was diluted 1000 times, and 10 ng/L of Rh internal standard was added to correct the signal drift. The solution was then shaken in a clean plastic centrifuge tube and analyzed by Agilent 7500CX ICP-MS instrument (Liu et al., 2020).

4.3 Sr-Nd isotopes

Whole-rock powder for Sr and Nd isotope analyses was dissolved in a Savillex Teflon cup, to which 2 mL 22N HF and 1 mL 8N HNO_3 solutions were added, then heated under a 120°C hot plate for 5–7 d to completely dissolve. After drying the sample again, a volume of 3 mL HNO_3 was added to dissolve sample for 2 h. Sr was separated with a SR-B50-A (100–150 μm) resin. Rare-earth elements (REEs) were separated with AG50-X8 cation exchange resin, and Nd was purified by HDEHP resin. The Sr and Nd were measured using a Neptune Plus multicollector (MC)-ICP-MS instrument. During the analysis period, the Rb-Sr and Sm-Nd blanks were <300 pg and <100 pg, respectively. The isotope ratio was adjusted to $^{88}\text{Sr}/^{86}\text{Sr}=8.375209$ and $^{146}\text{Nd}/^{144}\text{Nd}=0.7219$ to correct for mass fractionation. During the analysis period, instrument stability was assessed using the international standard samples NBS-987 and JNd-1. The measured values for the NBS-987 Sr and JNd-1 Nd standards were $^{87}\text{Sr}/^{86}\text{Sr}=0.71029413$ (± 0.000016) ($n=40$, 2SD (standard deviation)) and $^{143}\text{Nd}/^{144}\text{Nd}=0.51208068$ (± 0.000008) ($n=40$, 2SD), respectively. United States Geological Survey reference material BHVO-2 was measured to monitor the accuracy of the analytical procedures, with the following results: $^{87}\text{Sr}/^{86}\text{Sr}=0.703549$ (± 0.000008) and $^{143}\text{Nd}/^{144}\text{Nd}=0.512965$ (± 0.000004) (Liu et al., 2020).

The U-Pb zircon dating, major elements, trace elements, and Sr and Nd isotope data are presented in Tables 1, 2, and 3.

5 Results

5.1 Zircon U-Pb geochronology

Basaltic andesite (19MY-03) and diorite (19MY-05) were chosen for zircon U-Pb dating in this study, and the results are presented in Table 1. Zircon grains from the basaltic andesite and diorite samples are pale yellow in color, transparent to translucent, with spindly euhedral or stubby prismatic shapes and lengths ranging from 50 to 150 μm . The CL images show that all of the grains possess clear oscillatory zoning (Fig. 5).

Zircon grains from the basaltic andesite have U contents varying from 111×10^{-6} to 671×10^{-6} and Th contents varying from 98×10^{-6} to 314×10^{-6} , as well as Th/U ratios between 0.3 and 1.1 (Table 1), suggesting a magmatic origin for the zircons (Williams, 2001). Fifteen analyses yield $^{206}\text{Pb}/^{238}\text{U}$ ages ranging from 339 to 325 Ma, with a weighted mean $^{206}\text{Pb}/^{238}\text{U}$ age of 334 (± 4) Ma (mean square of weighted deviate (MSWD)=0.24; Fig. 5a).

Zircon grains from the diorite have U and Th contents varying from 161×10^{-6} to 2589×10^{-6} and from 60×10^{-6} to 1056×10^{-6} , respectively, and Th/U ratios of 0.1–0.8 (Table 1), suggesting a magmatic origin for the zircons (Williams, 2001). Twenty-nine analyses give $^{206}\text{Pb}/^{238}\text{U}$ ages ranging from 337 to 330 Ma, with a weighted mean $^{206}\text{Pb}/^{238}\text{U}$ age of 334 (± 1) Ma (MSWD=0.14; Fig. 5c).

In a chondrite-normalized REE diagram, trace-element contents of zircon grains from samples 19MY-03 and 19MY-05 display enrichment in heavy REEs (HREEs), strong positive Ce anomalies (Ce/Ce^* in the range of 4.61–199.00), and negative Eu anomalies (Eu/Eu^* ranging from 0.19 to 0.67) (Fig. 5b and d, respectively). In U/Yb vs Hf. diagrams (Grimes et al., 2007), data for both samples were plotted in the field of oceanic crust (Fig. 5e).

5.2 Major- and trace-element compositions

Major- and trace-element contents were determined for 10 samples of the Mayile volcanic and intrusive rocks (Table 2). Values of LOI range from 0.92 to 2.93, suggesting that any alteration of the samples was negligible. In a total-alkali-silica (TAS) diagram (Fig. 6a) (Bas et al., 1986), the magmatic rocks are classified mainly as basaltic andesite, andesite, dacite, and diorite, and in the Th vs. Co diagram (Fig. 6b) (Hastie et al., 2007), they belong to the calc-alkaline series. All samples have a wide range of SiO_2 (53.27%–66.98%), high Al_2O_3 (15.44%–21.03%), and moderate to low MgO (4.18%–1.62%) contents, moderate to low Mg# values (molar $\text{Mg}/[\text{Mg}+\text{Fe}^{2+}] \times 100$ ranging from 40 to 59), and low TiO_2 (0.50%–1.16%), CaO (2.60%–7.60%), and total Fe_2O_3 (TFe_2O_3) (4.08%–6.85%) contents. Total alkali ($\text{Na}_2\text{O}+\text{K}_2\text{O}$) contents range from 5.28% to 7.40%. The Rittmann Serial Index σ (1.28–3.48; $\sigma=(\text{K}_2\text{O}+\text{Na}_2\text{O})^2/(\text{SiO}_2-43)$) of samples is less than 4, indicating calc-alkaline affinity. In Harker diagrams, SiO_2 is negatively correlated with Al_2O_3 , TFe_2O_3 , MgO , and CaO (Fig. 7), suggesting that crystallization and separation of clinopyroxene, hornblende, and plagioclase occurred during magma evolution.

The analyzed samples show similar ranges of trace-element contents (Table 2). In a chondrite-normalized REE diagram (Fig. 8a), the samples display slight enrichment in light REEs (LREEs) and depletion in HREEs (La/YbN ranging from 2.99 to 7.83). Total REE content (ΣREEs) range from 59.5×10^{-6} to 108.5×10^{-6} and lie between contents of enriched mid-ocean ridge basalt (E-MORB) and ocean island basalt (OIB). The samples show insignificant negative Eu anomalies (Eu/Eu^* in the range of 0.74–1.12), indicating limited plagioclase fractionation. In a primitive-mantle-normalized incompatible-element diagram (Fig. 8b), all samples show enrichment in large-ion lithophile elements (LILEs; e.g., Rb, Ba, Th, and U) and depletion in high-field-strength elements (HFSEs; e.g., Nb, Ta, and Ti), which are typical characteristics of rocks from subduction-related arcs. The marked positive Sr anomalies of the samples, in contrast to those of OIB and mid-ocean ridge basalt (MORB), further indicate that limited plagioclase fractionation occurred in the magma residue and/or that seawater alteration took place.

Table 1 LA-ICP-MS zircon U-Pb isotopic analysis of the basaltic andesite and diorite for Mayile magmatic rocks in West Junggar

Sample spot	Isotopic content			Isotopic ratio			Age (Ma)									
	Th ($\times 10^{-6}$)	U ($\times 10^{-6}$)	Th/U	$^{207}\text{Pb}/^{206}\text{Pb}$	1 σ	$^{206}\text{Pb}/^{235}\text{U}$	1 σ	$^{207}\text{Pb}/^{238}\text{U}$	1 σ	$^{207}\text{Pb}/^{235}\text{U}$	1 σ	$^{206}\text{Pb}/^{238}\text{U}$	1 σ			
19MY-03	98	121	0.8	0.0568	0.0036	0.4132	0.0253	0.0531	0.0008	483	136	351	18	334	5	
	02	136	0.8	0.0547	0.0025	0.3877	0.0172	0.0516	0.0007	467	104	333	13	325	4	
	03	164	0.9	0.0562	0.0035	0.4084	0.0242	0.0535	0.0010	461	136	348	17	336	6	
	04	207	0.7	0.0526	0.0026	0.3849	0.0188	0.0534	0.0006	322	113	331	14	336	4	
	05	145	0.9	0.0563	0.0028	0.3709	0.0206	0.0534	0.0007	209	134	320	15	335	5	
	06	252	0.9	0.0566	0.0026	0.4295	0.0186	0.0525	0.0006	587	90	363	13	330	4	
	07	241	1.0	0.0544	0.0021	0.4300	0.0149	0.0540	0.0006	546	86	363	11	339	4	
	08	232	0.9	0.0514	0.0024	0.3771	0.0175	0.0533	0.0006	261	107	325	13	335	4	
	09	78.3	1.1	0.0687	0.0044	0.4865	0.0286	0.0534	0.0009	900	133	403	20	335	5	
	10	314	2.99	1.1	0.0494	0.0023	0.3607	0.0164	0.0534	0.0006	169	109	313	12	335	4
	11	247	2.90	0.9	0.0565	0.0026	0.4072	0.0176	0.0534	0.0007	472	102	347	13	335	4
	12	309	3.02	1.0	0.0598	0.0023	0.3755	0.0174	0.0535	0.0006	232	104	324	13	336	4
	13	270	827	0.3	0.0561	0.0025	0.4123	0.0185	0.0533	0.0014	457	100	351	13	334	8
	14	281	267	1.1	0.0573	0.0035	0.4232	0.0258	0.0536	0.0008	502	133	358	18	337	5
	15	104	186	0.6	0.0551	0.0040	0.3972	0.0261	0.0535	0.0009	417	156	340	19	336	6
19MY-05	01	40	123	2.90	0.0503	0.0021	0.3665	0.0151	0.0534	0.0007	209	98	317	11	335	4
	02	22	60	1.70	0.0598	0.0031	0.4363	0.0229	0.0532	0.0007	598	113	368	16	334	4
	03	139	466	8.63	0.0550	0.0014	0.4034	0.0103	0.0533	0.0004	409	62	344	7	335	3
	04	135	443	928	0.0495	0.0013	0.3627	0.0089	0.0532	0.0004	172	61	314	7	334	2
	05	118	371	862	0.0535	0.0013	0.3941	0.0104	0.0532	0.0005	350	86	337	8	334	3
	06	36	125	237	0.0564	0.0027	0.4086	0.0184	0.0532	0.0007	478	101	348	13	334	4
	07	150	511	968	0.0511	0.0015	0.3743	0.0105	0.0532	0.0004	256	67	323	8	334	3
	08	83	270	584	0.0546	0.0017	0.3966	0.0122	0.0530	0.0005	394	69	339	9	333	3
	09	106	299	934	0.0530	0.0014	0.3884	0.0099	0.0532	0.0004	328	27	333	7	334	3
	10	81	239	702	0.0528	0.0015	0.3873	0.0108	0.0533	0.0005	320	65	332	8	335	3
	11	181	614	1189	0.0505	0.0011	0.3711	0.0075	0.0533	0.0003	217	48	320	6	334	2
	12	278	950	1823	0.0544	0.0011	0.4004	0.0081	0.0532	0.0004	387	44	342	6	334	2
	13	31	94	205	0.0582	0.0028	0.4210	0.0193	0.0532	0.0007	600	106	357	14	334	4
	14	171	497	1269	0.0521	0.0011	0.3839	0.0082	0.0532	0.0003	300	48	330	6	334	2
	15	225	767	1346	0.0524	0.0012	0.3845	0.0092	0.0532	0.0030	302	56	330	7	333	2
	16	142	572	515	0.0533	0.0018	0.3935	0.0132	0.0533	0.0005	343	76	337	10	335	3
	17	126	451	889	0.0489	0.0018	0.3573	0.0126	0.0533	0.0007	146	85	310	9	335	4
	18	23	72	161	0.0589	0.0036	0.4195	0.0250	0.0531	0.0008	565	131	356	18	334	5
	19	318	895	2587	0.0540	0.0012	0.3993	0.0099	0.0532	0.0005	372	52	341	7	334	3
	20	115	371	722	0.0524	0.0023	0.4060	0.0156	0.0531	0.0006	428	88	346	11	333	4
	21	83	427	0.0517	0.0017	0.3819	0.0124	0.0536	0.0006	272	76	328	9	337	3	
	22	135	486	912	0.0501	0.0014	0.3681	0.0101	0.0532	0.0005	211	67	318	7	334	3
	23	227	714	1548	0.0583	0.0016	0.4275	0.0135	0.0525	0.0004	543	66	361	10	330	3
	24	19	60	161	0.0579	0.0033	0.4171	0.0238	0.0532	0.0009	524	131	354	17	334	5

Note: LA-ICP-MS, Laser Ablation Inductively Coupled Plasma Mass Spectrometer.

Table 2 Major and trace element compositions of Mayile magmatic rocks in West Junggar

Sample (Rock type)	MY53 (Basaltic andesite)	MY54 (Basaltic andesite)	MY55 (Basaltic andesite)	19MY43 (Basaltic andesite)	MY44 (Andesite)	19MY-06 (1) (Dacite)	19MY-06 (2) (Dacite)	MY50 (Diorite)	19MY-05 (Diorite)
Major element (%)									
SiO ₂	51.80	57.80	61.70	58.70	60.90	62.90	65.70	64.30	61.40
TiO ₂	0.85	1.14	0.61	1.19	0.76	0.89	0.76	0.80	0.72
Al ₂ O ₃	20.40	18.50	17.50	18.50	16.30	16.60	14.90	15.30	16.90
Fe ₂ O ₃ T	6.62	6.47	5.45	6.33	5.77	5.83	6.69	6.79	6.06
MnO	0.13	0.13	0.12	0.10	0.10	0.11	0.15	0.17	0.09
MgO	4.07	2.88	2.54	2.08	2.59	2.06	1.93	2.05	2.79
CaO	7.38	5.89	2.55	5.69	5.38	4.45	3.10	4.35	4.14
Na ₂ O	5.29	3.93	5.32	4.22	3.79	4.78	4.55	3.97	4.97
K ₂ O	0.52	1.29	1.93	1.96	1.51	1.30	1.14	1.26	1.59
P ₂ O ₅	0.12	0.21	0.16	0.20	0.23	0.20	0.14	0.16	0.10
LOI	2.93	1.97	2.36	1.05	2.86	0.92	1.09	0.98	2.61
Total	100.00	100.00	100.00	100.00	100.00	100.00	100.00	100.00	100.00
Mg# [#]	58.90	50.90	52.10	43.40	51.20	45.10	40.20	41.20	51.80
σ	3.48	1.78	2.74	2.39	1.51	1.83	1.41	1.28	1.49
Na ₂ O+K ₂ O	5.98	5.31	7.40	6.24	5.44	6.13	5.74	5.28	5.45
Trace element ($\times 10^{-6}$)									
Ti	5250	6954	3734	7225	4652	5405	4614	4845	4454
V	108	97.1	86.1	93.4	151	90.7	143	159	119
Cr	47.2	22.6	23.0	14.5	27.7	14.9	19.5	20.6	38.7
Co	17.5	19.1	14.0	13.6	20.8	10.8	14.0	24.8	12.3
Ni	34.3	15.5	19.0	8.07	34.6	10.8	8.83	7.51	29.2
Cu	11.7	15.9	9.92	20.9	146	32.8	26.0	58.5	21.4
Zn	71.0	56.3	65.6	59.7	107	40.7	74.2	91.6	44.5
Ga	19.6	29.3	41.6	28.8	24.0	33.0	20.3	22.1	36.3
Rb	6.03	9.28	33.0	35.1	42.5	11.9	26.0	31.9	29.0
Sr	717	594	598	398	910	431	370	360	513
Y	12.8	14.2	10.8	23.1	21.0	13.2	32.9	43.0	13.8
Zr	162	133	100	173	144	87.5	110	137	99
Nb	4.55	6.33	5.40	6.56	4.90	4.42	3.70	4.57	4.24
Ba	195	389	552	359	700	434	449	447	475

To be continued

Continued

Sample (Rock type)	MY53 (Basaltic andesite)	MY54 (Basaltic andesite)	MY55 (Basaltic andesite)	MY56 (Basaltic andesite)	19MY-03 (Basaltic andesite)	MY44 (Andesite)	19MY-06 (1) (Dacite)	19MY-06 (2) (Dacite)	MY50 (Diorite)	19MY-05 (Diorite)
La	11.0	11.5	12.4	14.2	17.7	11.4	11.6	16.1	9.41	12.3
Ce	28.1	26.1	26.7	29.3	39.7	24.2	28.2	36.0	23.0	30.5
Pr	3.32	3.25	2.99	4.20	4.87	3.02	3.70	4.80	2.77	3.28
Nd	13.3	13.3	11.6	17.2	20.3	12.3	16.9	21.8	11.3	13.7
Sm	2.95	2.99	2.36	4.11	4.16	2.81	4.47	5.54	2.70	3.10
Eu	0.94	1.09	0.84	1.25	0.98	0.85	1.24	1.37	0.87	0.73
Gd	2.52	2.98	2.21	3.98	3.63	2.59	4.63	5.84	2.59	2.79
Tb	0.42	0.46	0.34	0.67	0.56	0.41	0.81	1.00	0.41	0.45
Dy	2.38	2.74	1.97	4.12	3.29	2.37	5.11	6.32	2.52	2.62
Ho	0.49	0.56	0.41	0.86	0.65	0.49	1.06	1.32	0.53	0.51
Er	1.30	1.50	1.11	2.36	1.79	1.33	2.96	3.75	1.41	1.38
Tm	0.21	0.25	0.19	0.38	0.27	0.21	0.45	0.57	0.24	0.21
Yb	1.30	1.49	1.25	2.41	1.62	1.32	2.77	3.49	1.41	1.26
Lu	0.19	0.23	0.18	0.36	0.25	0.20	0.43	0.54	0.22	0.19
Hf	3.76	4.19	3.27	5.26	3.34	2.84	2.54	3.15	3.42	2.78
Ta	0.34	0.44	0.43	0.45	0.33	0.32	0.20	0.28	0.33	0.36
Pb	11.10	7.25	9.54	7.44	7.13	6.57	13.80	9.15	2.79	7.93
Th	3.90	2.58	3.36	3.46	3.00	2.04	1.77	2.13	2.66	2.20
U	1.34	1.17	1.11	1.26	0.98	0.87	0.50	0.66	0.94	0.73
^a (La/Yb) _N	6.07	5.54	7.12	4.24	7.83	6.21	2.99	3.31	4.79	7.01
^a (Gd/Yb) _N	1.60	1.65	1.46	1.37	1.85	1.63	1.38	1.39	1.52	1.83
Eu/Eu*	1.06	1.12	1.12	0.95	0.77	0.96	0.83	0.74	1.01	0.76
REE	68.40	68.40	64.60	85.50	99.70	63.50	84.40	109.00	59.50	73.00
LREE	59.60	58.20	56.90	70.30	87.60	54.60	66.10	85.70	50.10	63.60
HREE	8.81	10.20	7.65	15.20	12.10	8.91	18.20	22.80	9.33	9.41
LREE/HREE	6.76	5.71	4.64	7.43	7.26	6.12	3.63	3.75	5.37	6.76

Note: LOI, loss on ignition; Mg[#], molar Mg/[Mg+Fe²⁺]^{1/2}×100 assuming Fe²⁺O²⁻/FeO=0.15; Eu/Eu*=Eu_N/(Sm_N×Gd_N)^{1/2}; REE, rare earth element; LREE, light rare earth element; HREE, heavy rare earth element.^a Chondrite normalizing values are from (Sun and McDonough, 1989).

Table 3 Sr and Nd isotope ratios and Rb, Sr, Sm, and Nd contents of representative Mayile magmatic rocks in West Junggar

Rock type	19MY-03-1 (Basaltic andesite)	19MY-03-2 (Basaltic andesite)	19MY-06 (1) (Dacite)	19MY-06 (2) (Dacite)	19MY-05 (Diorite)
Rb ($\times 10^{-6}$)	42.5	42.5	26.0	31.9	15.6
Sr ($\times 10^{-6}$)	910	910	370	360	767
Sm ($\times 10^{-6}$)	4.16	4.16	4.47	5.54	3.10
Nd ($\times 10^{-6}$)	20.3	20.3	16.9	21.8	13.7
$^{87}\text{Rb} / ^{86}\text{Sr}$	0.130520	0.130520	0.195676	0.247256	0.056824
$^{87}\text{Sr} / ^{86}\text{Sr}$	0.704271	0.704383	0.705941	0.705733	0.704477
$\pm 2\sigma$	0.000027	0.000010	0.000009	0.000012	0.000010
$^{87}\text{Sr} / ^{86}\text{Sr}_{(t)}$	0.703649	0.703761	0.705008	0.704554	0.704207
$^{147}\text{Sm} / ^{144}\text{Nd}$	0.126246	0.126246	0.162308	0.156245	0.138599
$^{143}\text{Nd} / ^{144}\text{Nd}$	0.512798	0.512790	0.512809	0.512802	0.512779
$\pm 2\sigma$	0.000003	0.000006	0.000003	0.000006	0.000004
$^{143}\text{Nd} / ^{144}\text{Nd}_{(t)}$	0.512521	0.512513	0.512453	0.512459	0.512476
$\varepsilon_{\text{Nd}(t)}$	6.1	6.0	4.8	4.9	5.2
$T_{\text{DM1}} (\text{Ma})$	616	630	1016	927	755
$f_{\text{Sm/Nd}}$	-0.36	-0.36	-0.17	-0.21	-0.30

Note: $^{87}\text{Sr} / ^{86}\text{Sr}$ and $^{87}\text{Sm} / ^{86}\text{Nd}$ ratios were calculated using Rb, Sr, Sm, and Nd contents (Table 2). Measured $^{87}\text{Sr} / ^{86}\text{Sr}$ was corrected to mass fractionation using $^{88}\text{Sr} / ^{86}\text{Sr} = 8.375209$. Strontium standard NBS-987 was used to monitor instrumental performance and yielded an average $^{87}\text{Sr} / ^{86}\text{Sr}$ ratio of 0.710294 (± 0.000016) ($n=60$, 2SD). SD, standard deviation. The measured $^{146}\text{Nd} / ^{144}\text{Nd}$ and fractionation-corrected $^{143}\text{Nd} / ^{144}\text{Nd}$ ratios of the JNd1-1 standard were $^{87}\text{Sr} / ^{86}\text{Sr} = 0.710294$ (± 0.000016) ($n=40$, 2SD) and $^{143}\text{Nd} / ^{144}\text{Nd} = 0.512081$ (± 0.000008) ($n=40$, 2SD), respectively. All measured Nd isotopic ratios were normalized to $^{146}\text{Nd} / ^{144}\text{Nd} = 0.7219$.

5.3 Sr–Nd isotope compositions

Five whole-rock samples were analyzed for Sr and Nd isotopes, and results for Sr and Nd isotopic ratios and Sr, Rb, Sm, and Nd elemental abundances are presented in Table 3. The covariation in initial Sr and Nd isotope ratios is shown in Figure 9. Although the initial Sr ratios ($^{87}\text{Sr} / ^{86}\text{Sr}_{(t)}$) of the five samples show a wide range from 0.703649 to 0.705008, they have relatively uniform ($^{143}\text{Nd} / ^{144}\text{Nd}_{(t)}$) ratios of 0.512779–0.512809, $\varepsilon_{\text{Nd}(t)}$ values ranging from 4.8 to 6.2, and young depleted-mantle Nd model ages (T_{DM}) varying from 1016 to 616 Ma, indicating that these rocks were derived from a depleted-mantle source. The whole-rock Nd–Sr isotopic systematics (Fig. 9) are similar to those of rocks from Vanuatu island arc (Beaumais et al., 2016) and the volcanic rocks from West Junggar (Geng et al., 2011).

6 Discussion

6.1 Petrogenesis and mantle source

Major element contents of Mayile volcanic and intrusive rocks indicate calc-alkaline series affinity and are characterized by moderate MgO contents (1.62%–4.18%) and Mg# values (40–59), and low Cr (14.5×10^{-6} – 47.2×10^{-6}) and Ni (7.5×10^{-6} – 34.6×10^{-6}) contents. The major element variation of Mayile samples is due to fractional crystallization. For example, the decrease in Al_2O_3 , TiFe_2O_3 , MgO, and CaO with increasing SiO_2 (Fig. 7) suggest the volcanic and intrusive rocks derived from a parental magma through crystallization of clinopyroxene, hornblende, and plagioclase. These contents, together with the trace-element characteristics, enrichment in LREEs and LILEs, and depletion in HFSEs, are consistent with those of modern Vanuatu island arc (Beaumais et al., 2016) (Fig. 8), with all of these features indicating that the studied rocks were formed from typical subduction-zone island-arc magma (Pearce and Peate, 1995). The studied volcanic and intrusive rocks have similar trace-element patterns (Fig. 8) and comparable Sr–Nd isotopic values, implying that they were derived from a depleted-mantle source and same parental magma.

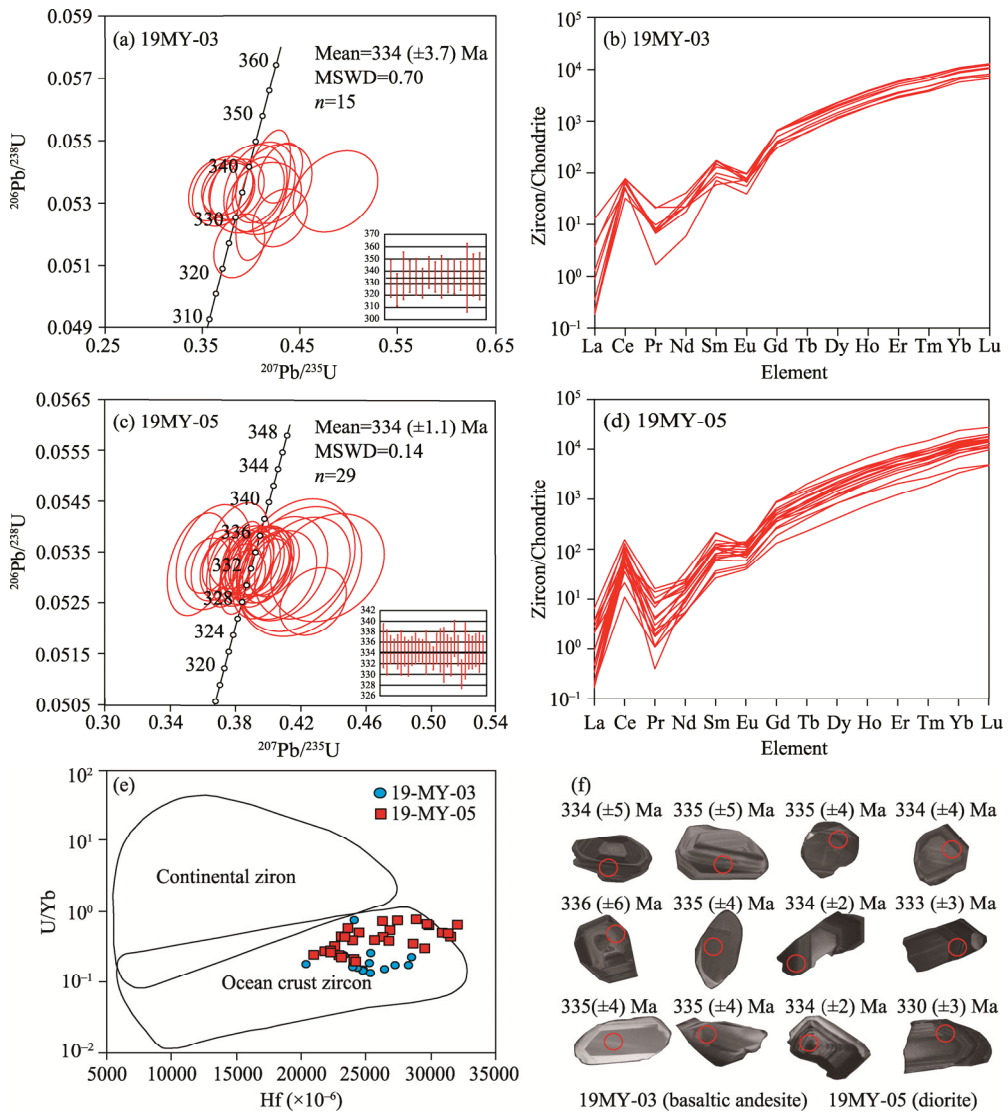


Fig. 5 U-Pb concordia diagrams (a, c), chondrite-normalized REEs patterns (b, d) (Sun and McDonough, 1989), U/Yb vs. Hf diagrams (e) (Grimes et al., 2007), and representative cathodoluminescence (CL) images for zircons from the Mayile magmatic rocks (f). REEs, rare-earth elements; MSWD, mean square of weighted deviate.

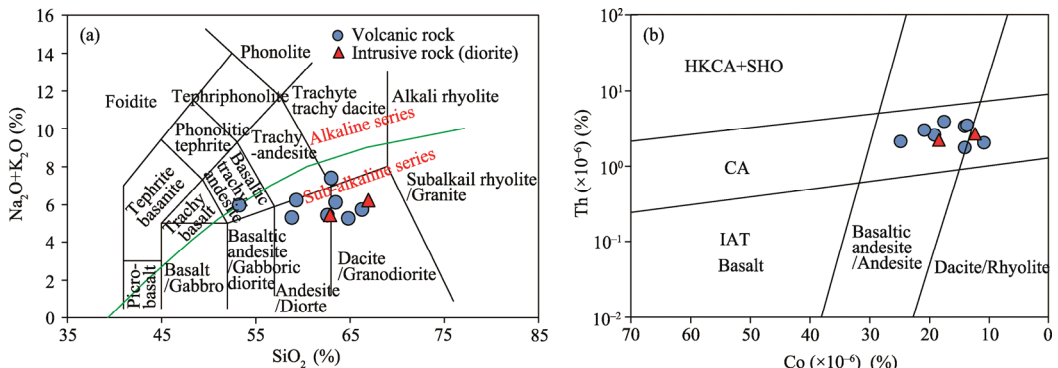


Fig. 6 Classification diagrams for Mayile magmatic rocks: (a) TAS diagram after Bas et al. (1986) and (b) Th vs. Co (Hastie et al., 2007) discrimination diagram of the analyzed samples showing geochemical classification of Mayile volcanic rocks and their intrusive rocks. CA, calc-alkaline series; HKCA, high-potassium calc-alkaline series; IAT, island arc tholeiite; SHO, shoshonite.

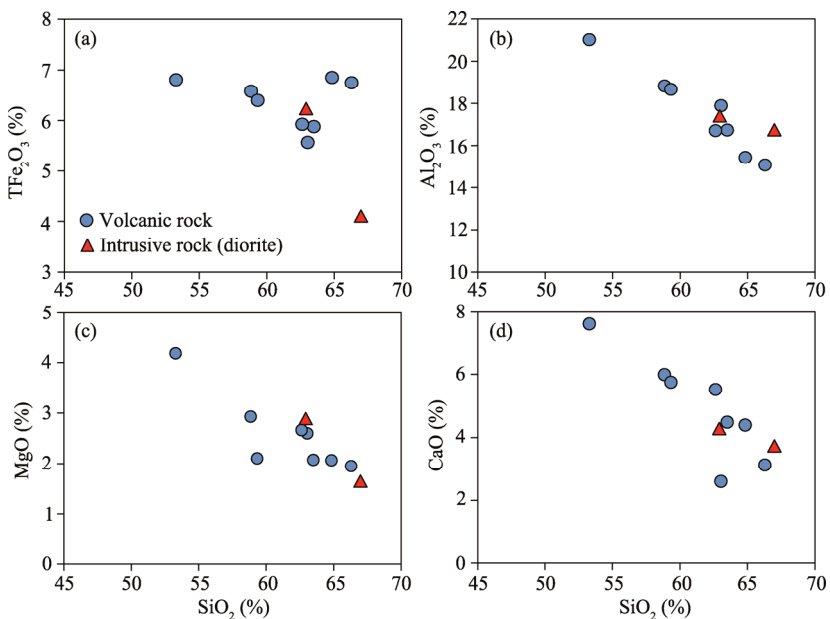


Fig. 7 SiO_2 versus TFe_2O_3 (a), Al_2O_3 (b), MgO (c), and CaO (d) Harker diagrams for Early Carboniferous volcanic and intrusive rocks from Mayile area

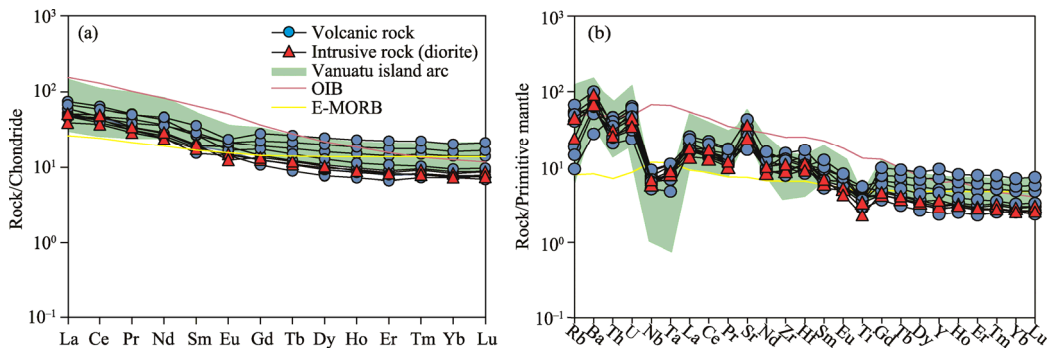


Fig. 8 Chondrite-normalized (a) and primitive-mantle-normalized (b) trace-element patterns for volcanic and intrusive rocks from the Mayile area. Chondrite and primitive mantle values are from Sun and McDonough (1989). Vanuatu island arc sample data are from Beaumais et al. (2016). Values of OIB (ocean island basalt) and E-MORB (enriched mid-ocean ridge basalt) used are from Sun and McDonough (1989).

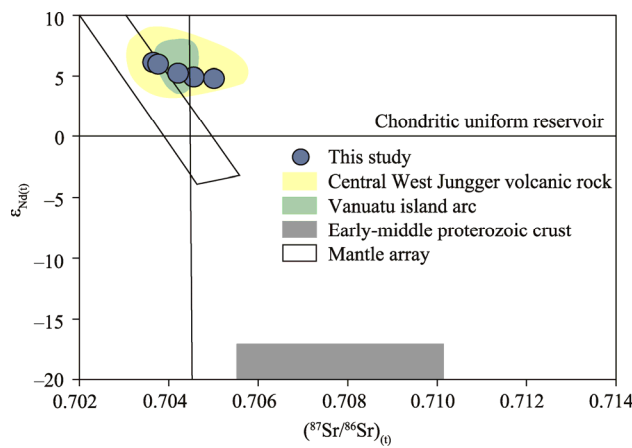


Fig. 9 Age-corrected ($t=334$ Ma) $\epsilon_{\text{Nd}(t)}$ versus $^{87}\text{Sr}/^{86}\text{Sr}(t)$ ratios for Mayile volcanic and intrusive rocks compared with those for central West Junggar volcanic rocks and Vanuatu island arc rocks (Geng et al., 2011;

Beaumais et al., 2016). Data for early to middle Proterozoic crust are from Hu et al. (2000).

Many studies have shown that incompatible elements (e.g., HFSEs and HREEs) are conservative (or immobile) elements whose contribution from the slab to the mantle wedge is minimal (Pearce and Cann, 1973; Pearce and Peate, 1995). Therefore, Zr, Nb, and Y can be used to discriminate the nature of the magma source (Pearce and Cann, 1973). The Mayile volcanic and intrusive rocks have low Nb and Zr contents, which, together with low Nb/Zr ratios, indicate magma with depleted-mantle features (Fig. 10a). For understanding petrogenesis, partial melting in the mantle source with different garnet and spinel contents should be reflected in La/Sm vs. La by curves with distinct trajectories (Aldanmaz et al., 2000). In diagrams of La/Sm vs. La (Fig. 10b), the Mayile samples were plotted mostly between the melting path of garnet and spinel lherzolite, indicating that the rocks were originated from 10% to 25% degree of partial melting of garnet and spinel lherzolite (Fig. 10b).

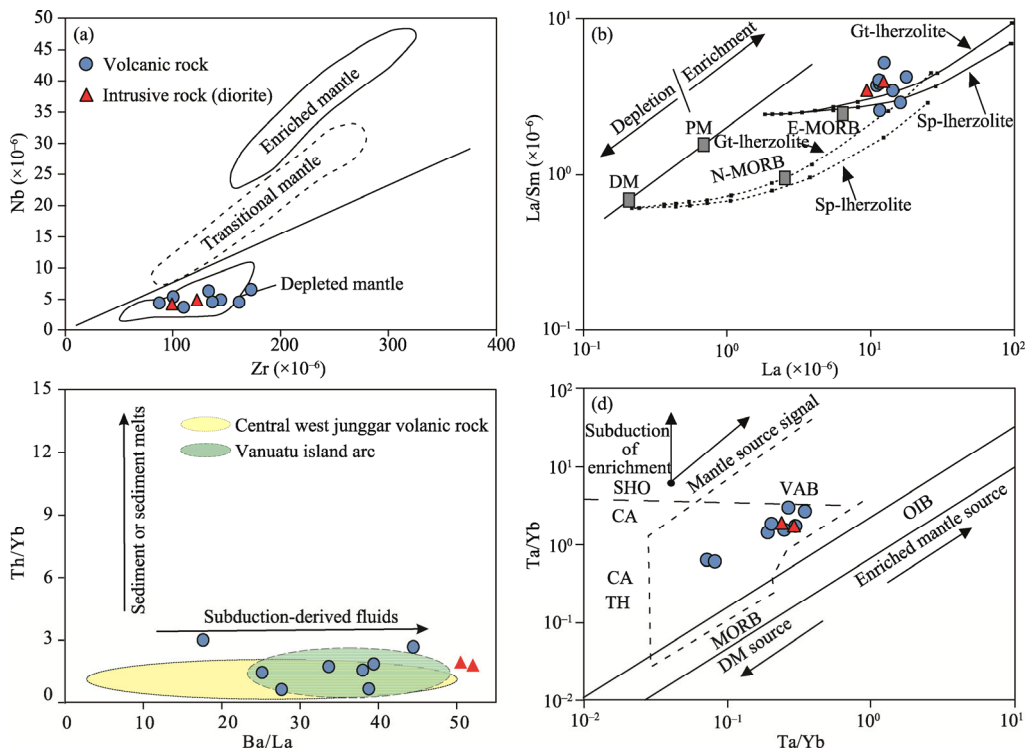


Fig. 10 Diagrams of Nb vs. Zr (a), La/Sm vs. La (after Aldanmaz et al. (2000)) (b), Th/Yb vs. Ba/La (c), and Th/Yb vs. Ta/Yb (d) (after Pearce (1983)) for Mayile magmatic rocks. N-MORB, normal mid-ocean ridge basalt; E-MORB, enriched mid-ocean ridge basalt; DM, depleted mantle; PM, primitive mantle; MORB, mid-ocean ridge basalt; OIB, ocean island basalt; VAB, volcanic arc basalt; CA, calk alkaline; TH, tholiite; SHO, shoshonite.

Ratios of incompatible trace elements have been used to constrain the petrogenesis and mantle source of igneous rocks (Pearce and Peate, 1995). Since Th, Yb, and Ta are HFSEs that are immobile in fluids, Th/Yb and Ta/Yb ratios of these elements are largely independent of variations caused by the degree of partial melting and crystal fractionation, and therefore reflect the degree of depletion or enrichment of the mantle source (Pearce and Peate, 1995; Hawkesworth and Kemp, 2006). Importantly, Th is enrichment in marine sediments and highly soluble in melt, while Ba is mobile in fluids, thus, ratios of Ba/La can indicate the contribution of subduction-derived fluid (s), and Th/Yb ratios can indicate sediment melt contribution (Pearce and Peate, 1995). Mayile rocks displaying a wide range of Ba/La for a given Th/Yb suggests that the subduction components were dominated by subduction-derived fluids, which is similar to the features of central West Junggar volcanic rocks and Vanuatu island arc rocks (Geng et al., 2011; Beaumais et al., 2016) (Fig. 10c). In the Th/Yb vs. Ta/Yb diagram (Fig. 10d), Mayile rocks show

a higher Th/Yb for a given Ta/Yb compared with MORB–OIB array, indicating a mantle source also enriched by addition of melt from subducted sediments and showing the geochemical characteristics of island-arc magmatic rocks. Thus, Mayile volcanic and intrusive rocks were probably produced by mixing subducted fluids and sediment melt to the depleted mantle.

Furthermore, all of the samples have low $(^{87}\text{Sr}/^{86}\text{Sr})_{\text{t}}$ ratios (range of 0.7038–0.7050 and mean of 0.7042) with positive $\epsilon_{\text{Nd(t)}}$ values (range of 4.8–6.2 and mean of 5.4) and young T_{DM} Nd model ages ranging from 1016 to 616 Ma, which are isotopic characteristics that indicate a depleted-mantle origin and clearly differ from characteristics of crust-derived continental arc rocks. Moreover, $\epsilon_{\text{Nd(t)}}$ and $(^{87}\text{Sr}/^{86}\text{Sr})_{\text{t}}$ systematics (Fig. 9) for the samples show that these rocks plot close to the mantle array and show similar isotopic features to those of volcanic rocks from central West Junggar (Geng et al., 2011) and modern Vanuatu intra-oceanic arc rocks (Beaumais et al., 2016), suggesting that they likely share a similar petrogenesis to that of intra-oceanic arc magmatic rocks.

To summarize, trace-element contents and isotopic compositions show that the parental magma of Mayile volcanic and intrusive rocks had a depleted-mantle source and might have been derived by partial melting of subduction-related modified sub-arc mantle, specifically, a garnet and spinel peridotite mantle source.

6.2 Tectonic implications

A reasonable tectonic interpretation for the Mayile volcanic and intrusive rocks should account not only for their variable petrological and geochemical features but also for the tectonic evolution of Junggar Ocean region during the Carboniferous. All of Mayile volcanic rock samples are plotted in the calc-alkaline basalt field (CAB) in an Hf/3–Th–Ta diagram (Wood et al., 1979) (Fig. 11a). The studied diorites are plotted in the volcanic-arc granite (VAG) field in a Rb vs. (Y+Nb) diagram (Fig. 11b). In zircon U/Yb vs. Hf and U/Yb vs. Y discrimination diagrams (Grimes et al., 2007), Mayile magmatic rocks belong to oceanic crust (Fig. 5). Thus, the geochemical characteristics of Mayile volcanic and intrusive rocks indicate that their genesis and tectonic setting are related to intra-oceanic crust subducted arc magmatism.

The tectonic evolution of West Junggar during the Carboniferous is debated, because the study on the Carboniferous arc magmatism associated with Junggar oceanic plate subduction in southern West Junggar is insufficient. Paleomagnetic studies showed that the Junggar Ocean between Junggar island arc and Yili plate existed until the Late Carboniferous (Wang et al., 2007a). Therefore, a subduction setting continued to dominate West Junggar during the Carboniferous (Long et al., 2006; Wang et al., 2007b). The normal subduction calc-alkaline magmatism dominated during the Early Carboniferous. For example, Zircon U–Pb dating of volcanic rocks in Baogutu and Miaoergou regions of southern West Junggar has shown that northwestward intra-oceanic subduction of Junggar oceanic plate occurred during 344–331 Ma (Buckman and Aitchison, 2004; Geng et al., 2011). The ridge subduction-related magmatism, as represented by adakitic rock, high-Mg andesites, enriched- or high-Nb basaltic rocks, charnockites, and alkali-feldspar granite (Geng et al., 2009; Tang et al., 2010; Yin et al., 2010), commenced and took place between 331 and 310 Ma and probably lasted into the latest Carboniferous (302 Ma), as evidenced by the Darbut E-MORB type basalts (Liu et al., 2009). Wu et al. (2018) proposed that subduction of Junggar oceanic plate started during the Early Devonian and continued to the Late Carboniferous (310 Ma), with subsequent post-collisional tectonic processes continuing to the latest Carboniferous (302 Ma). However, Han et al. (2006) considered that the time frame of post-collisional magmatic activity in northern Xinjiang extended from 330 to 250 Ma. Xu et al. (2019) reported ages of 309 to 303 Ma for the Miaoergou granitoids and 304–295 Ma for the equivalent rhyolites, and proposed that a tectonic transition from oceanic subduction to collision in southern West Junggar occurred during the Late Carboniferous–Early Permian. Based on the above studies, we infer that southern West Junggar was dominated by normal subduction during the Early Carboniferous (Fig. 12a) and by ridge subduction and/or subsequent post-collision processes during the Late Carboniferous–Early Permian (Fig. 12b). Our study yielded U–Pb ages of around 334 Ma (Early Carboniferous) for the intra-oceanic arc

magmatism represented by Mayile volcanic and intrusive rocks, making them coeval with arc plutonic and volcanic rocks of southern West Junggar (Shen et al., 2009; Guo et al., 2010; Geng et al., 2011; Xu et al., 2012; Liu et al., 2017), which were generated in association with northwestward subduction of Junggar oceanic plate (Geng et al., 2011).

Our new results, combined with those of previous studies, allow us to propose a model for the Carboniferous tectonic evolution of West Junggar (Fig. 12). During the Early Carboniferous, northwestward subduction of Junggar oceanic plate led to partial melting of the sub-arc mantle. This caused Mayile intra-oceanic arc magmatism to occur in southern West Junggar, as evidenced by the studied basaltic andesites, dacites, and diorites. After this period of normal subduction, ridge subduction occurred during the Late Carboniferous, following which Junggar Ocean closed gradually from the Late Carboniferous to Early Permian during the post-collision stage (Xiao et al., 2003; Liu et al., 2017; Xu et al., 2019).

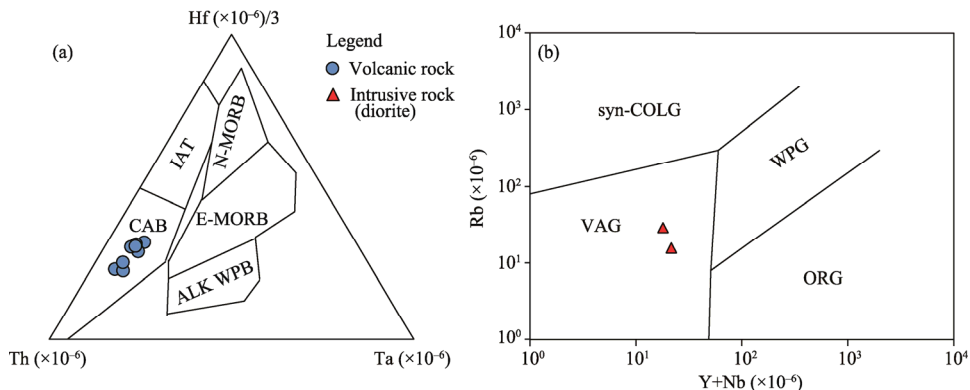


Fig. 11 Hf/3-Th-Ta diagram (after Wood et al. (1979)) for Mayile volcanic rocks (a), and Rb vs. Y+Nb diagram (after Pearce (1996)) for Mayile intrusive rocks (b). N-MORB, normal mid-ocean ridge basalt; E-MORB, enriched mid-ocean ridge basalt; ALK WPB, alkali within-plate basalt; IAT, island-arc tholeites; CAB, calc-alkaline basalts; syn-COLG, post-collisional granite; VAG, volcanic-arc granite; WPG, within-plate granite; ORG, ocean ridge granite.

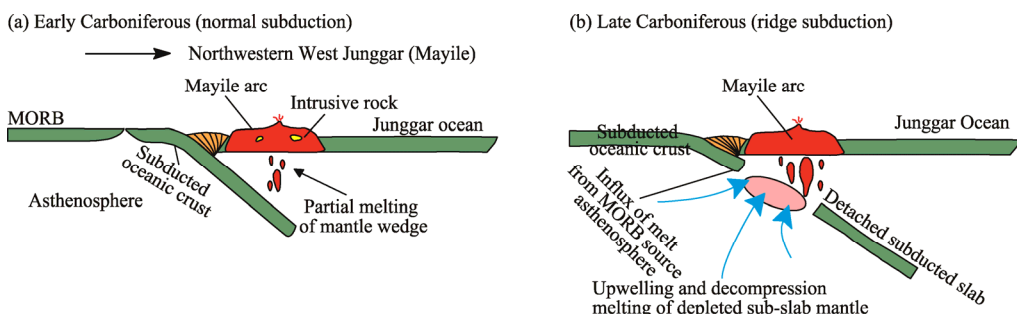


Fig. 12 Proposed tectonic model for the Carboniferous magmatic province in West Junggar (Mayile). Regional tectonic model was from Jahn et al. (2004), Xiao et al. (2009), and Liu et al. (2017a). Slab window model was from Tang et al. (2010) and Geng et al. (2011). (a), Early Carboniferous: Junggar oceanic plate subducts northwestward during normal subduction; (b), Late Carboniferous: formation of a slab window in Junggar Ocean owing to subduction of a spreading ridge.

7 Conclusions

In this study, we carry the new geochronological, major- and trace-element, and Sr–Nd isotopic analyses on Mayile volcanic and intrusive rocks from the southern West Junggar region. The results show that LA-ICP-MS zircon U–Pb dating of Mayile basaltic andesite and diorite yield a crystallization age of 334 Ma, implying that these volcanic and intrusive rocks were formed during the Early Carboniferous. The rocks are calc-alkaline and are characterized by enrichment

in LILEs and LREEs and depletion in HREEs, indicating that they were formed from typical subduction-zone island-arc setting. Their Sr-Nd isotopic compositions indicate a depleted-mantle source that underwent partial melting of 10%–25% garnet and spinel lherzolite. We suggest that southern West Junggar region was located in an intra-oceanic arc setting related to northwestward subduction of Junggar oceanic plate during the Early Carboniferous.

Acknowledgements

This study was jointly supported by the CAS "Light of West China" Program (2018-XBYJRC-003), the National Natural Science Foundation of China (41772059, 92055208), the Guangxi Natural Science Foundation for Distinguished Young Scholars, China (2018GXNSFFA281009), and the Fifth Bagui Scholar Innovation Project of Guangxi Zhuang Autonomous Region, China. We are grateful for editor's excellent editorial handling and constructive comments from two anonymous reviewers, which substantially improved the final presentation of the manuscript. This is a contribution to International Geoscience Programme (IGCP) 662 and Guangxi Key Mineral Resources Deep Exploration Talent Highland.

References

Aldanmaz E, Pearce J A, Thirlwall M F, et al. 2000. Petrogenetic evolution of late Cenozoic, post-collision volcanism in western Anatolia, Turkey. *Journal of Volcanology and Geothermal Research*, 102(1–2): 67–95.

Bas M J L, Maitre R W L, Streckeisen A, et al. 1986. A chemical classification of volcanic rocks based on the Total Alkali-Silica diagram. *Journal of Petrology*, 27(3): 745–750.

Beaumais A, Bertrand H, Chazot G, et al. 2016. Temporal magma source changes at Gaua volcano, Vanuatu island arc. *Journal of Volcanology and Geothermal Research*, 322: 30–47.

Buckman S, and Aitchison J C. 2004. Tectonic evolution of Palaeozoic terranes in West Junggar, Xinjiang, NW China. *Geological Society, London, Special Publications*, 226(1): 101–129.

Chen B, and Jahn B M. 2004. Genesis of post-collisional granitoids and basement nature of the Junggar Terrane, NW China: Nd-Sr isotope and trace element evidence. *Journal of Asian Earth Sciences*, 23(5): 691–703.

Chen B, and Arakawa Y. 2005. Elemental and Nd-Sr isotopic geochemistry of granitoids from the West Junggar foldbelt (NW China), with implications for Phanerozoic continental growth. *Geochimica et Cosmochimica Acta*, 69(5): 1307–1320.

Chen J F, Han B F, Ji J Q, et al. 2010. Zircon U-Pb ages and tectonic implications of Paleozoic plutons in northern West Junggar, North Xinjiang, China. *Lithos*, 115(1–4): 137–152.

Choulet F, Faure M, Cluzel D, et al. 2013. Architecture and evolution of accretionary orogens in the Altaiids collage: The early Paleozoic West Junggar (NW China). *American Journal of Science*, 312(10): 1098–1145.

Coleman R G. 1989. Continental growth of northwest China. *Tectonics*, 8(3): 621–635.

Du H Y, Chen J F, Ma X, et al. 2019. Origin and tectonic significance of the Hoboksar ophiolitic mélange in northern West Junggar (NW China). *Lithos*, 336–337: 293–309.

Feng Y, Coleman R G, Tilton G, et al. 1989. Tectonic evolution of the west Junggar region, Xinjiang, China. *Tectonics*, 8(4), 729–752.

Filippova I B, Bush V A, and Didenko A N. 2002. Middle Paleozoic subduction belts: The leading factor in the formation of the Central Asian fold-and-thrust belt. *Russian Journal of Earth Sciences*, 3(6): 405–426.

Gao J, Li M S, Xiao X C, et al. 1998. Paleozoic tectonic evolution of the Tianshan Orogen, northwestern China. *Tectonophysics*, 287(1): 213–231.

Geng H Y, Sun M, Yuan C, et al. 2009. Geochemical, Sr-Nd and zircon U-Pb-Hf isotopic studies of Late Carboniferous magmatism in the West Junggar, Xinjiang: Implications for ridge subduction? *Chemical Geology*, 266(3–4): 364–389.

Geng H Y, Sun M, Yuan C, et al. 2011. Geochemical and geochronological study of early Carboniferous volcanic rocks from the West Junggar: Petrogenesis and tectonic implications. *Journal of Asian Earth Sciences*, 42(5): 854–866.

Grimes C B, John B E, Kelemen P B, et al. 2007. Trace element chemistry of zircons from oceanic crust: A method for distinguishing detrital zircon provenance. *Geology*, 35(7): 643–646.

Gu P Y, Li Y J, Zhang B, et al. 2009. LA-ICP-MS zircon U-Pb dating of gabbro in the Darbut ophiolite, West Junggar, China. *Acta Petrologica Sinica*, 25(6): 1364–1372. (in Chinese)

Guo L S, Liu Y L, Wang Z H, et al. 2010. The zircon U-Pb LA-ICP-MS geochronology of volcanic rocks in Baogutu areas, western Junggar. *Acta Geologica Sinica (English Edition)*, 26(2): 471–477.

Han B F, Ji J Q, Song B, et al. 2006. Late Paleozoic vertical growth of continental crust around the Junggar Basin, Xinjiang, China (Part I): Timing of post-collisional plutonism. *Acta Petrologica Sinica* (5): 1077–1086. (in Chinese)

Han B F, Guo Z J, Zhang Z C, et al. 2010. Age, geochemistry, and tectonic implications of a late Paleozoic stitching pluton in the North Tian Shan suture zone, western China. *Geological Society of America Bulletin*, 122(3–4): 627–640.

Hastie A R, Kerr A C, Pearce J A, et al. 2007. Classification of altered volcanic island arc rocks using immobile trace elements: development of the Th–Co discrimination diagram. *Journal of Petrology*, 48(12): 2341–2357.

Hawkesworth C J, and Kemp A I S. 2006. The differentiation and rates of generation of the continental crust. *Chemical Geology*, 226(3–4): 134–143.

Hu A Q, Jahn B M, Zhang G X, et al. 2000. Crustal evolution and Phanerozoic crustal growth in northern Xinjiang: Nd isotopic evidence. Part I. Isotopic characterization of basement rocks. *Tectonophysics*, 328(1–2): 15–51.

Jahn B M, Wu F Y, and Chen B. 2000a. Massive granitoid generation in Central Asia: Nd isotope evidence and implication for continental growth in the Phanerozoic. *Episodes*, 23(2): 82–92.

Jahn B M, Griffin W L, and Windley B. 2000b. Continental growth in the Phanerozoic: Evidence from Central Asia. *Tectonophysics*, 328(1–2): VII–X.

Jahn B M, Capdevila R, Liu D, et al. 2004. Sources of Phanerozoic granitoids in the transect Bayanhongor-Ulaan Baatar, Mongolia: geochemical and Nd isotopic evidence, and implications for Phanerozoic crustal growth. *Journal of Asian Earth Sciences*, 23(5): 629–653.

Jian P, Liu D Y, Yuruo S, et al. 2005. SHRIMP dating of SSZ ophiolites from northern Xinjiang, China: implications for generation of oceanic crust in the central Asian orogenic belt. In: Sklyarov E V. *Structural and Tectonic Correlation across the Central Asia Orogenic Collage: North-Eastern Segment. Guidebook and Abstract Volume of the Siberian Workshop ICCP-480*. Institute of the Earth's Crust, Siberian Branch, Russian Academy of Science, Irkutsk, 246.

Khain E V, Bibikova E V, Salnikova E B, et al. 2003. The Palaeo-Asian ocean in the Neoproterozoic and early Palaeozoic: new geochronologic data and palaeotectonic reconstructions. *Precambrian Research*, 122(1–4): 329–358.

Kroner A, Hegner E, Lehmann B, et al. 2008. Palaeozoic arc magmatism in the Central Asian Orogenic Belt of Kazakhstan: SHRIMP zircon ages and whole-rock Nd isotopic systematics. *Journal of Asian Earth Sciences*, 32(2–4): 118–130.

Liu B, Han B F, Ren R, et al. 2017. Petrogenesis and tectonic implications of the Early Carboniferous to the Late Permian Barleik plutons in the West Junggar (NW China). *Lithos*, 272–273: 232–248.

Liu X J, Xu J F, Wang S Q, et al. 2009. Geochemistry and dating of E-MORB type mafic rocks from Dalabute ophiolite in West Junggar, Xinjiang and geological implications. *Acta Petrologica Sinica*, 25(6): 1373–1389. (in Chinese)

Liu X J, Xiao W J, Xu J F, et al. 2017. Geochemical signature and rock associations of ocean ridge-subduction: Evidence from the Karamaili Paleo-Asian ophiolite in east Junggar, NW China. *Gondwana Research*, 48: 34–49.

Liu X J, Zhang Z G, Xu J F, et al. 2020. The youngest Permian Ocean in Central Asian Orogenic Belt: Evidence from geochronology and geochemistry of Bingdaban Ophiolitic Mélange in Central Tianshan, northwestern China. *Geological Journal*, 55(3): 2062–2079.

Long X P, M S, C Y, et al. 2006. Genesis of Carboniferous volcanic rocks in the eastern Junggar: constraints on the closure of the Junggar Ocean. *Acta Petrologica Sinica*, (1): 31–40. (in Chinese)

Ludwig K R. 2003. User's manual for a geochronological toolkit for Microsoft Excel (Isoplot/Ex version 3.0). Berkeley Geochronology Center, Special Publication, 4: 1–71.

Pearce J. 1983. Role of the sub-continental lithosphere in magma genesis at active continental margin. In: Hawkesworth C J, Norry M J. *Continental Basalts and Mantle Xenoliths*. Nantwich, Cheshire: Shiva Publications, 230–249.

Pearce J, and Peate D. 1995. Tectonic implications of the composition of volcanic arc magmas. *Annual Review of Earth and Planetary Sciences*, 23(1): 251–285.

Pearce J. 1996. Sources and settings of granitic rocks. *International Union of Geological Sciences*, 19(4): 120–125.

Pearce J A, Cann J R. 1973. Tectonic setting of basic volcanic rocks determined using trace element analyses. *Earth and Planetary Science Letters*, 19(2): 290–300.

Ren R, Han B F, Xu Z, et al. 2014. When did the subduction first initiate in the southern Paleo-Asian Ocean: New constraints from a Cambrian intra-oceanic arc system in West Junggar, NW China. *Earth and Planetary Science Letters*, 388: 222–236.

Safonova I, Biske G, Romer R L, et al. 2016. Middle Paleozoic mafic magmatism and ocean plate stratigraphy of the South Tianshan, Kyrgyzstan. *Gondwana Research*, 30: 236–256.

Safonova I Y, Buslov M M, Simonov V A, et al. 2011. Geochemistry, petrogenesis and geodynamic origin of basalts from the Katun' accretionary complex of Gorny Altai (southwestern Siberia). *Russian Geology and Geophysics*, 52(4): 421–442.

Sengör A M C, Natal'in B A, Burtman V S. 1993. Evolution of the Altai tectonic collage and Palaeozoic crustal growth in Eurasia. *Nature*, 364(6435): 299–307.

Sengör A M C, Natal'in B A. 1996. Turkic-type orogeny and its role in the making of the continental crust. *Annual Review of Earth and Planetary Sciences*, 24(1): 263.

Shen P, Shen Y C, Liu T B, et al. 2009. Geochemical signature of porphyries in the Baogutu porphyry copper belt, western Junggar, NW China. *Gondwana Research*, 16(2): 227–242.

Sun W D, McDonough W. 1989. Chemical and isotopic systematics of oceanic basalts: Implications for mantle composition and processes. London: Geological Society, Special Publications, 42(1): 313–345.

Tang G J, Wang Q, Wyman D A, et al. 2010. Ridge subduction and crustal growth in the Central Asian Orogenic Belt: Evidence from Late Carboniferous adakites and high-Mg diorites in the western Junggar region, northern Xinjiang (west China). *Chemical Geology*, 277(3–4): 281–300.

Wang B, Shu L S, Cluzel D, et al. 2007a. Geochemical constraints on Carboniferous volcanic rocks of the Yili Block (Xinjiang, NW China): Implication for the tectonic evolution of Western Tianshan. *Journal of Asian Earth Sciences*, 29(1): 148–159.

Wang Q, Wyman D A, Zhao Z H, et al. 2007b. Petrogenesis of Carboniferous adakites and Nb-enriched arc basalts in the Alataw area, northern Tianshan Range (western China): Implications for Phanerozoic crustal growth in the Central Asia orogenic belt. *Chemical Geology*, 236(1–2): 42–64.

Wang Z H, Sun S, Li J L, et al. 2003. Paleozoic tectonic evolution of the northern Xinjiang, China: Geochemical and geochronological constraints from the ophiolites. *Tectonics*, 22(2), doi: 10.1029/2002TC001396.

Williams I S. 2001. Response of detrital zircon and monazite, and their U–Pb isotopic systems, to regional metamorphism and host–rock partial melting, Cooma Complex, southeastern Australia. *Australian Journal of Earth Sciences*, 48(4): 557–580.

Windley B F, Alexeiev D, Xiao W J, et al. 2007. Tectonic models for accretion of the Central Asian Orogenic Belt. *Journal of the Geological Society*, 164(1): 31–47.

Wood D A, Joron J L, and Treuil M. 1979. A re-appraisal of the use of trace elements to classify and discriminate between magma series erupted in different tectonic settings. *Earth and Planetary Science Letters*, 45(2): 326–336.

Wu C, Hong T, Xu X W, et al. 2018. Tectonic evolution of the Paleozoic Barluk continental arc, West Junggar, NW China. *Journal of Asian Earth Sciences*, 160: 48–66.

Xiao W J, Windley B F, Hao J, et al. 2003. Accretion leading to collision and the Permian Solonker suture, Inner Mongolia, China: Termination of the central Asian orogenic belt. *Tectonics*, 22(6): 1069.

Xiao W J, Pirajno F, and Seltmann R. 2008a. Geodynamics and metallogeny of the Altai orogen. *Journal of Asian Earth Sciences*, 32(2–4): 77–81.

Xiao W J, Han C M, Yuan C, et al. 2008b. Middle Cambrian to Permian subduction-related accretionary orogenesis of Northern Xinjiang, NW China: Implications for the tectonic evolution of central Asia. *Journal of Asian Earth Sciences*, 32(2–4): 102–117.

Xiao W J, Windley B F, Yuan C, et al. 2009. Paleozoic multiple subduction-accretion processes of the southern Altaiids. *American Journal of Science*, 309(3): 221–270.

Xiao W J, Mao Q G, Windley B F, et al. 2010a. Paleozoic multiple accretionary and collisional processes of the Beishan orogenic collage. *American Journal of Science*, 310(10): 1553–1594.

Xiao W J, Huang B C, Han C, et al. 2010b. A review of the western part of the Altaiids: A key to understanding the architecture of accretionary orogens. *Gondwana Research*, 18(2–3): 253–273.

Xiao W J, and Santosh M. 2014. The western Central Asian Orogenic Belt: A window to accretionary orogenesis and continental growth. *Gondwana Research*, 25(4): 1429–1444.

Xiao W J, Windley B F, Sun S, et al. 2015. A tale of amalgamation of three Permo-Triassic collage systems in Central Asia: oroclines, sutures, and terminal accretion. *Annual Review of Earth and Planetary Sciences*, 43(1): 477–507.

Xinjiang Bureau of Geology and Mineral Resources (XBGMR). 1993. *Regional Geology of Xinjiang Uygur Autonomy Region*. Beijing: Geology Publishing House, 1–841. (in Chinese)

Xu Q Q, Ji J Q, Zhao L, et al. 2013. Tectonic evolution and continental crust growth of Northern Xinjiang in northwestern China: Remnant ocean model. *Earth-Science Reviews*, 126: 178–205.

Xu S L, Chen X H, Li T D, et al. 2019. Time of the ocean-continent transition in West Junggar: Constraints from zircon U–Pb dating and Lu–Hf isotopic composition. *Geology in China*, 46(05): 1061–1078.

Xu X, He G Q, Li H Q, et al. 2006. Basic characteristics of the Karamay ophiolitic melange, Xinjiang, and its zircon SHRIMP dating. *Geology in China*, 33(3): 470–475.

Xu Z, Han B F, Ren R, et al. 2012. Palaeozoic multiphase magmatism at Barleik Mountain, southern West Junggar, Northwest China: implications for tectonic evolution of the West Junggar. *International Geology Review*, 55(5): 633–656.

Yakubchuk A S, Shatov V V, Kirwin D, et al. 2005. Gold and base metal metallogeny of the Central Asian orogenic supercollage. In: Hedenquist J W, Thompson J F H, Goldfarb R J, et al. *Economic Geology*. Littleton, CO: Society of

Economic Geologists.

Yang G X, Li Y J, Santosh M, et al. 2012. A Neoproterozoic seamount in the Paleoasian Ocean: Evidence from zircon U-Pb geochronology and geochemistry of the Mayile ophiolitic mélange in West Junggar, NW China. *Lithos*, 140–141: 53–65.

Yang G X, Li Y J, Xiao W J, et al. 2015. OIB-type rocks within West Junggar ophiolitic mélanges: Evidence for the accretion of seamounts. *Earth-Science Reviews*, 150: 477–496.

Yang G X, Li Y J, Tong L L, et al. 2020. An Early Cambrian plume-induced subduction initiation event within the Junggar Ocean: Insights from ophiolitic mélanges, arc magmatism, and metamorphic rocks. *Gondwana Research*, 88: 45–66.

Yang Y Q, Zhao L, Zheng R G, et al. 2019. Evolution of the early Paleozoic Hongguleleng–Balkybey Ocean: Evidence from the Hebukesaier ophiolitic mélange in the northern West Junggar, NW China. *Lithos*, 324–325: 519–536.

Yin J Y, Yuan C, Sun M, et al. 2010. Late Carboniferous high-Mg dioritic dikes in Western Junggar, NW China: Geochemical features, petrogenesis and tectonic implications. *Gondwana Research*, 17(1): 145–152.

Zhang J E, Xiao W J, Han C M, et al. 2011. A Devonian to Carboniferous intra-oceanic subduction system in Western Junggar, NW China. *Lithos*, 125(1–2): 592–606.

Zhang J E, Xiao W J, Luo J, et al. 2018. Collision of the Tacheng block with the Mayile-Barleik-Tangbale accretionary complex in Western Junggar, NW China: Implication for Early–Middle Paleozoic architecture of the western Altaids. *Journal of Asian Earth Sciences*, 159: 259–278.